Journal of Materials Chemistry A

PAPER

View Article Online
View Journal | View Issue

CrossMark click for updates

Cite this: J. Mater. Chem. A, 2016, 4, 10314

Robust 3D nanowebs assembled from interconnected and sandwich-like C@Fe_3O_4@C coaxial nanocables for enhanced Li-ion storage†

Yan Wang,[a] Qunting Qu,*[a] Yuyao Han,[a] Tian Gao,[a] Jie Shao,*[b] Zhichen Zuo,[c] Weijie Liu,[a] Qiang Shi[a] and Honghe Zheng*[a]

Received 15th April 2016
Accepted 2nd June 2016

DOI: 10.1039/c6ta03118h

www.rsc.org/MaterialsA

An ideal electrode material of Li-ion batteries (LIBs) is expected to not only involve nanoscale subunits, but also possess a stable 3D porous hierarchical microstructure. Herein, a green and bottom-up approach is developed for fabricating robust 3D nanowebs assembled from interlinked and sandwich-like carbon@Fe_3O_4@carbon coaxial nanocables. The uniform growth of iron oxide precursors on carbon substrates is achieved with the assistance of a layer-by-layer assembled polyelectrolyte, which is demonstrated to be a strategy applicable to the preparation of various carbon-based functional composites. The carbon components of the hybrid materials are *in situ* doped with nitrogen due to the utilization of nitrogen-containing polymers as carbon sources. In such rationally nanoengineered materials, the 3D nitrogen-doped carbon nanowebs can provide a continuous pathway for electron transport, reduce the diffusion length of Li-ions, and improve the structural integrity and stability of the whole electrode. Accordingly, the obtained materials exhibit impressive Li-storage properties including high capacity, long cycle life, and superior rate performance.

Published on 02 2016. Downloaded by Fail Open on 23.07.25 10:02:10.

Introduction

Nanoengineering of carbon-based hybrids has become one of the most powerful means to improve the electrochemical performance of electrode materials in rechargeable Li-ion batteries (LIBs).[1–5] In the carbon-based hybrids of unique architecture, particularly those of a sandwich-like architecture with carbon distributed on both sides, each component not only plays its own role but also functions synergistically to store Li ions.[6–10] The carbon matrix provides fast electron conduction pathways and serves as the skeleton to improve the structural stability of the whole electrode.[11–13] The uniform distribution of the other active components on the carbon scaffold facilitates fast Li^+ storage and release.[14–16] In addition to the construction of a unique architecture, nitrogen doping of the carbon matrix is another effective method to improve the electrochemical performance since the electronic conductivity and interfacial stability of the hybrids can be greatly increased.[17–21] Despite these achievements, the carbon supports used for the preparation of carbon-based hybrids usually need to be specially treated such as reflux with acids to improve their coupling ability, which will not only sacrifice the electrical conductivity of carbon but also cause severe environmental pollution.[22] The development of an environmentally friendly, simple, and general strategy is still urgently necessary to prepare nitrogen-doped carbon-based hybrids of a sandwich-like architecture.

Among the various anode candidates for LIBs, ferroferric oxide (Fe_3O_4) has aroused increasing interest due to its advantages of high theoretical capacity (926 mA h g^{-1}), natural abundance, and environmental friendliness.[23–26] Nonetheless, Fe_3O_4 is based on a conversion reaction mechanism, and the accompanied volume expansion and shrinkage of electrode materials during lithiation/delithiation processes result in severe electrode pulverization and integrity loss of the electrode. As a result, Fe_3O_4 usually exhibits poor cycling stability. Moreover, it is difficult to form a stable solid electrolyte interphase (SEI) layer on Fe_3O_4, leading to a continuous consumption of the electrolyte and low coulombic efficiency during charge/discharge.[27,28] To tackle these issues, many attempts have been focused on the preparation of carbon/Fe_3O_4 nanocomposites, where the nanostructures of Fe_3O_4 were assembled onto or embedded into carbon matrices such as graphene and carbon nanotubes.[29–33] Another effective strategy is to rationally engineer a robust three-dimensional (3D) architecture assembled from Fe_3O_4 nanobuilding blocks, which synergistically combines the advantages of both nanostructures and

[a]College of Physics, Optoelectronics and Energy & Collaborative Innovation Center of Suzhou Nano Science and Technology, Soochow University, Suzhou, Jiangsu 215006, China. E-mail: qtqu@suda.edu.cn; hhzheng@suda.edu.cn

[b]College of Chemistry, Chemical Engineering and Material Science, Soochow University, Suzhou, Jiangsu 215006, China. E-mail: shaojie@suda.edu.cn

[c]Suzhou Power Capacitor Co., LTD, Suzhou, Jiangsu 215122, China

† Electronic supplementary information (ESI) available: SEM, high-resolution TEM, TG curves, and BET and electrochemical data of the obtained samples. See DOI: 10.1039/c6ta03118h

This journal is © The Royal Society of Chemistry 2016

Published on 02 2016. Downloaded by Fail Open on 23.07.25 10:02:10.

microstructures.[34,35] In such structures, the Li-ion transport length is much shorter than that in the bulk counterparts owing to the nanoscaled subunits, and meanwhile, the 3D architecture at the submicrometer or micrometer scale can effectively avoid the self-aggregation of active nanomaterials.[1] Therefore, it is highly desirable to prepare carbon/Fe_3O_4 hybrids not only involving nanometer-sized subunits but also possessing a stable 3D hierarchical microstructure.

In this study, a robust 3D nanoweb assembled from interconnected and sandwich-like carbon@Fe_3O_4@carbon coaxial nanocables is rationally designed and synthesized through a green and bottom-up approach. This unique 3D hierarchical architecture not only allows the fast transport of Li ions and electrons, but also benefits the structural stability and integrity of the electrode. Furthermore, the adoption of a nitrogen-containing polymer precursor results in the *in situ* nitrogen doping of the carbon components. As a consequence, the obtained carbon@Fe_3O_4@carbon hybrid exhibits a high reversible capacity (1263 mA h g^{-1}), good rate behavior (426 mA h g^{-1} at 10C), and negligible capacity loss after 150 continuous cycles.

Results and discussion

Lou's group[22] and our group[12] have separately demonstrated that carboxylated carbon nanotubes (CNTs) and sulfonated polymers could adsorb Fe^{3+} ions easily due to the coordination interactions. Afterwards, through the forced hydrolysis of Fe^{3+} ions, the β-FeOOH nanoneedles were *in situ* and uniformly assembled on the CNTs and the polymer backbones, respectively. The as-formed β-FeOOH could be easily transformed into Fe_2O_3 and Fe_3O_4 after calcination in air and Ar, respectively. It should be noted that, prior to the growth of β-FeOOH, the CNTs and polymers have to be treated with a strong acid to attach active functional groups onto their surfaces, and thereby enable the nucleation and anchoring of β-FeOOH. This strong acid-treatment process would cause great ecological damage to the environment. Additionally, Zhang and co-workers reported another acid-free strategy for the synthesis of core–shell structured CNT/Fe_2O_3 by virtue of a high-temperature and high-pressure process, which is energy consuming and also a potential safety hazard.[36] Herein, a new protocol for the green and facile preparation of sandwiched C@Fe_3O_4@C hybrids is proposed and schematically shown in Fig. 1. A 3D nitrogen-doped carbon nanoweb (NCW) prepared through the direct carbonization of a nanoweb-like polypyrrole (PPy) precursor is first used as the carbon matrix. The interconnected 3D carbon nanoweb is expected to provide a continuous pathway for electron transport and serve as a very stable backbone to improve the structural stability of the electrode. The 3D NCW is then coated with two layers of polyelectrolytes comprising of a positively charged poly(diallyldimethylammonium chloride) (PDDA) layer and a negatively charged poly(sodium 4-styrenesulfonate) (PSS) layer. The sequential layer-by-layer (LBL) deposition of PDDA and PSS endows the carbon matrix with a homogeneous distribution of negative charges on their surface, which subsequently facilitates the uniform adsorption of Fe^{3+} ions *via* an electrostatic attractive interaction.[13,37] Consequently, FeOOH is homogeneously grown on the NCW. The core–shell structured NCW@FeOOH is further coated with a thin and continuous polydopamine (PDA) layer through the *in situ* polymerization of dopamine. The catechol group of dopamine could form a strong binding affinity to the surface of FeOOH, so that a uniform and continuous polydopamine film can be easily obtained.[38] During the pyrolysis of NCW@FeOOH@PDA, PDA is transformed into a nitrogen-doped carbon shell (NCS),[39,40] and FeOOH is reduced to Fe_3O_4 by carbon. The robust 3D nanoweb assembled from cross-linked and sandwich-like NCW@Fe_3O_4@NCS coaxial nanocables can be finally fabricated. It is noteworthy that the procedures for the growth of FeOOH and PDA on NCW are performed in aqueous solutions and under mild reaction conditions, which is of great significance for large-scale and green synthesis.

The nanoweb-like PPy precursor was prepared according to a reported method but with a modified concentration of starting materials.[41] As seen in Fig. 2a and S1,† the PPy precursor presents a 3D open network structure, which is composed of highly interconnected nanofibers with an average diameter of 50 nm. It is also observed that the diameter of these nanofibers obtained at a low concentration of starting materials is smaller than that obtained at a high concentration (Fig. S2†). After carbonization of PPy, the NCW perfectly inherits the 3D

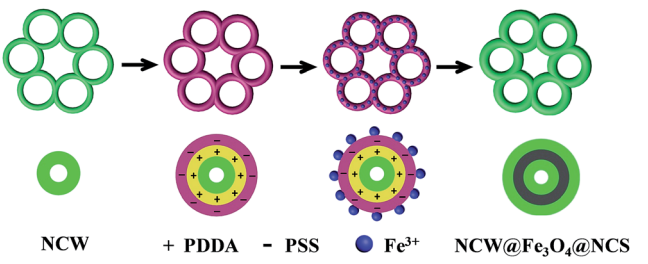

Fig. 1 Schematic illustration of the synthesis of a 3D nanoweb assembled from 1D NCW@Fe_3O_4@NCS nanocables.

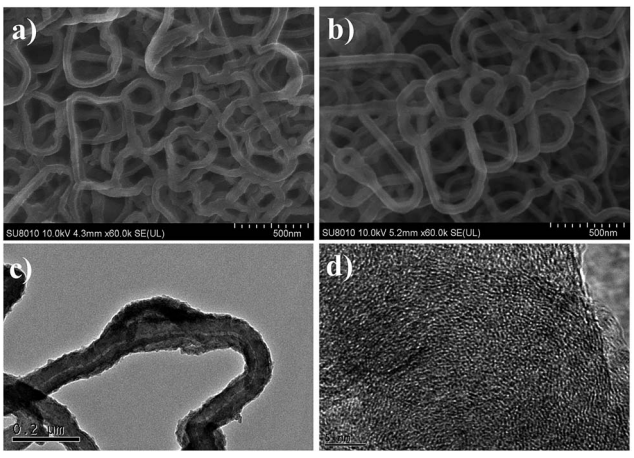

Fig. 2 SEM images of (a) a 3D nanoweb-like PPy precursor (b) NCW, and (c and d) TEM images of NCW at different magnifications.

Published on 02 2016. Downloaded by Fail Open on 23.07.25 10:02:10.

nanoweb morphology of the PPy precursor (see Fig. 2b). The preparation of the PPy precursor is simple and controllable, and the 3D carbon nanoweb can be easily obtained, which holds great promise for large-scale applications. The transmission electron microscopy (TEM) image of the NCW (Fig. 2c) indicates that the nanofibers of the NCW seem to consist of hollow interiors. In other words, the 3D NCW is assembled from 1D nanotubes. The formation of the nanotubular structures should mainly result from the decomposition of a cetrimonium bromide (CTAB)-based soft template upon calcination as indicated by the thermogravimetric (TG) curves of CTAB and the PPy precursor (Fig. S3†). The high-resolution TEM image of the NCW (Fig. 2d) not only shows the stacking of short-range ordered carbon layers, but also discloses that numerous micropores are randomly distributed within the NCW, which accounts for its high surface area of 150 $m^2 g^{-1}$ (Fig. S4†). The nanotubular and porous structure of the NCW could accelerate the mass transfer and shorten the diffusion pathway length of Li ions.

After the decoration of the NCW with two layers of polyelectrolytes, the morphology shows no obvious changes (Fig. S5†). The thickness of the polyelectrolyte layers is determined to be about 1–1.5 nm from the high-resolution TEM image (Fig. S6†). The outer layer of negatively charged PSS facilitates the rapid adsorption of large amounts of Fe^{3+} ions and the subsequent nucleation and growth of the FeOOH seed crystal. As a result, in the 3D nanoweb structure of NCW@FeOOH, the surfaces of the primary nanofibers are uniformly covered by a layer of nanocrystalline particles (SEM image in Fig. 3a). Meanwhile, the average diameter of these nanofibers increases to 80 nm due to the deposition of FeOOH. To elucidate the effect of the polyelectrolyte decoration, another NCW@FeOOH sample was prepared in the absence of polyelectrolytes. As shown in Fig. S7,† a serious aggregation of FeOOH nanoparticles is observed, demonstrating that the presence of polyelectrolytes can guarantee the uniform growth/distribution of FeOOH on the NCW. Such an LBL polyelectrolyte-assisted solution-based method is easy to operate, and applicable to the synthesis of a large variety of functional composites, which is further demonstrated by the successful syntheses of the other two 1D carbon/Fe_3O_4 hybrids with the assistance of polyelectrolytes (Fig. S8†).

The as-prepared nanoweb-like NCW@FeOOH is further coated with a layer of PDA by virtue of the strong adhesion of PDA onto FeOOH. As shown by the SEM image (Fig. 3b), the nanoparticle-like FeOOH is not as distinct as that observed before PDA coating. After calcination of NCW@FeOOH@PDA under the protection of an inert atmosphere, sandwich-like NCW@Fe_3O_4@NCS coaxial nanocables are obtained. SEM observations of the final product at different magnifications (Fig. 3c and d) show that the 3D nanoweb-like structure is perfectly preserved and Fe_3O_4 nanoparticles are homogenously distributed on the surface of the primary nanofibers. Since it is difficult to clearly observe the crystallite size of Fe_3O_4 as well as the thickness of the PDA-derived carbon shell from SEM images, TEM characterization is carried out. As shown in Fig. 4a and b, nanocrystallite-like Fe_3O_4 with a size of about 5–7 nm is uniformly anchored onto the 3D carbon nanoweb. Moreover, there are no isolated Fe_3O_4 nanoparticles in this sample, indicating that FeOOH preferentially nucleates and grows on the surfaces of the NCW with the aid of polyelectrolytes. Besides, it is observed that the entire surface of Fe_3O_4 nanocrystallites is surrounded by a continuous amorphous carbon shell with a thickness of 2–4 nm, which could suppress the abscission or dissolution of pulverized Fe_3O_4 upon electrochemical cycling. The selected-area electron diffraction (SAED) pattern of NCW@Fe_3O_4@NCS (Fig. 4c) exhibits five distinct diffraction rings with the *d*-values corresponding well to the (220), (311), (400), (511), and (440) crystalline planes of Fe_3O_4. To further illustrate the spatial distribution of Fe_3O_4 and carbon in the NCW@Fe_3O_4@NCS hybrid, energy-dispersive X-ray (EDX) line-scan analysis was performed along the diameter of 1D nanofibers as indicated by the green arrow in Fig. 4d. From Fig. 4e, we can see that the content of Fe presents two peaks at the

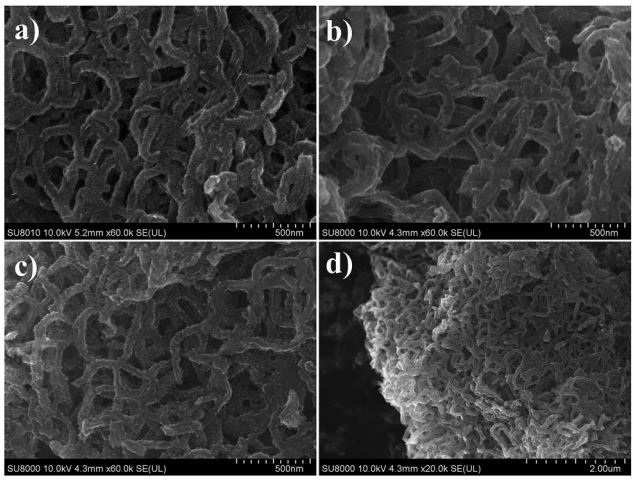

Fig. 3 SEM images of 3D nanoweb-like (a) NCW@FeOOH, (b) NCW@FeOOH@PDA, and (c and d) NCW@Fe_3O_4@NCS.

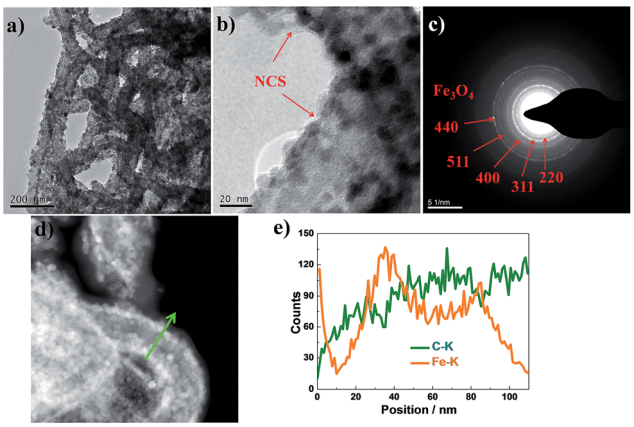

Fig. 4 (a and b) TEM images of NCW@Fe_3O_4@NCS at different magnifications, (c) the SAED pattern of NCW@Fe_3O_4@NCS, (d) annular dark-field image of NCW@Fe_3O_4@NCS, (e) EDX line-scan elemental distribution of NCW@Fe_3O_4@NCS along the direction of the green arrow indicated in (d).

 This journal is © The Royal Society of Chemistry 2016

Published on 02 2016. Downloaded by Fail Open on 23.07.25 10:02:10.

positions of 30 and 80 nm, which is consistent with the expected result since Fe_3O_4 is supposed to distribute on the surface of inner carbon nanofibers. Accordingly, the content evolution of C shows a slight decrease at the two places where the content of Fe is at its highest value, indicating that Fe_3O_4 is sandwiched between the inner NCW and outer NCS.

On the whole, the structure of NCW@Fe_3O_4@NCS can be described as a 3D nanoweb assembled from interconnected and sandwich-like coaxial nanocables.

The crystallographic structures of NCW and NCW@Fe_3O_4@NCS were investigated by powder X-ray diffraction (XRD) (Fig. 5a). The diffraction peak at about 25° is characteristic of the (002) crystalline plane of the carbon material. The broad and weak peaks of the NCW at this degree reflects the low graphitic degree of PPy-derived carbon, which should result from its high porosity and the large amounts of disorderly oriented graphitic-type fragments as observed from Fig. 2d. In the XRD pattern of NCW@Fe_3O_4@NCS, besides the broad peak of carbon, other distinct diffraction peaks can be well assigned to the face-centered cubic Fe_3O_4 (JCPDS no. 65-3107), implying the successful conversion of FeOOH to Fe_3O_4. The content of Fe_3O_4 in the NCW@Fe_3O_4@NCS hybrid is estimated to be about 68% through TG analysis (Fig. S9†). X-ray photoelectron spectroscopy (XPS) was used to analyze the elemental composition of the NCW matrix. The full survey spectrum in Fig. 5b demonstrates the existence of C, N, and O elements. The deconvoluted XPS spectra (inset of Fig. 5b) of N1s core level suggest the presence of three types of nitrogen in the NCW, namely graphitic (398.4 eV), pyrrolic (399.8 eV) and pyridinic (401.0 eV) nitrogen. The weight percentage of nitrogen in the NCW determined from the XPS spectra is 12.5%, revealing a quite high level of nitrogen doping by adopting the nitrogen-containing PPy as the precursor. The high-level of nitrogen-doping can enhance the electrochemical reactivity and electronic conductivity and facilitate Li-ion transport in the carbon core. Fourier transform infrared spectra (FTIR) of the NCW and NCW@Fe_3O_4@NCS (Fig. 5c) validate the presence of C–N (1403 cm^{-1}), C=C (1645 cm^{-1}), and N–H (3119 cm^{-1}) bonds, also suggesting the successful doping of nitrogen into the carbon matrix. The Raman spectra of the NCW and NCW@Fe_3O_4@NCS are compared in Fig. 5d. The two strong peaks at 1340 and 1570 cm^{-1} are associated with the disordered (D-band) and graphitic carbon (G-band), respectively. The relative intensity ratio of the D-band to G-band is 1.06, reflecting the presence of a large amount of disordered carbon in the NCW, which can be correlated to its porous structure and high nitrogen-doping amount. In contrast with the NCW, the new peaks at 214, 278, 390, and 588 cm^{-1} in the Raman spectra of NCW@Fe_3O_4@NCS correspond to the A_{1g} and E_g vibration modes of Fe_2O_3, which are normally observed for other Fe_3O_4-based materials due to the partial oxidation of Fe_3O_4 during Raman measurements.[42]

The Li-storage performance of 3D NCW@Fe_3O_4@NCS and the NCW was investigated using lithium foil as the counter electrode. Their initial three galvanostatic discharge/charge curves at a current density of 0.05C (1C = 1000 mA g^{-1}) within the voltage window of 0.01–3.0 V are shown in Fig. 6a and b, respectively. In contrast to the sloping voltage profiles of the NCW, the NCW@Fe_3O_4@NCS electrode exhibits a distinct and flat voltage plateau at 0.88 V during the first discharge, which originates from the conversion of Fe_3O_4 to Fe and Li_2O upon Li^+ intercalation.[6] The following charge process corresponds to the reversible oxidation from Fe^0 to Fe^{2+}/Fe^{3+} accompanied by Li^+ extraction. The coulombic efficiency of the NCW in the first cycle is 50%, suggesting a quite large irreversible capacity loss. This can be attributed to the porous structure of the NCW, which creates numerous active sites for the reductive decomposition reaction of the electrolyte. The first coulombic efficiency of NCW@Fe_3O_4@NCS is 69%, suggesting an increased reversibility of the hybrid material for Li^+ storage. With respect to the overall mass of the NCW@Fe_3O_4@NCS active material,

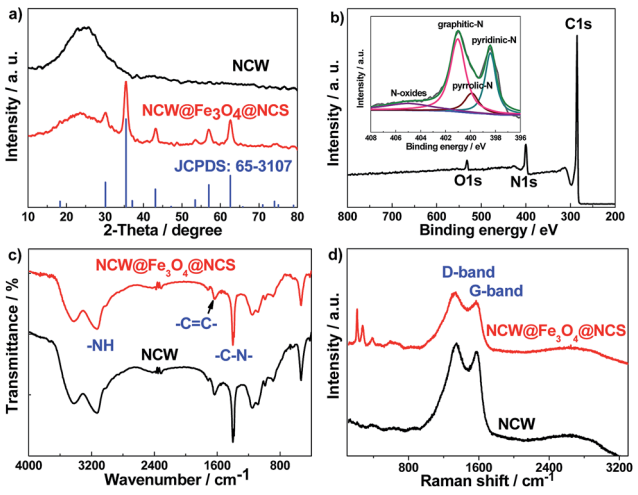

Fig. 5 (a) XRD patterns, (c) FTIR spectra, and (d) Raman spectra of the NCW and NCW@Fe_3O_4@NCS; (b) the full survey XPS spectrum of the NCW; the inset in (b) is the deconvoluted XPS spectra in the N1s core-level region.

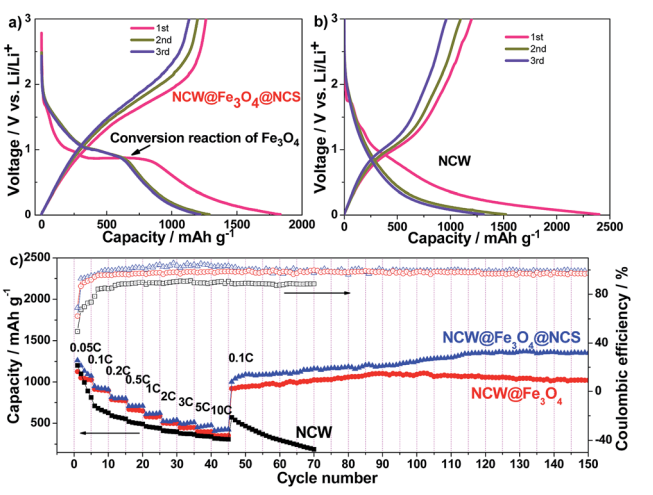

Fig. 6 The initial three galvanostatic discharge/charge curves of (a) NCW@Fe_3O_4@NCS and (b) the NCW; (c) the capacity evolution of NCW@Fe_3O_4@NCS, NCW@Fe_3O_4, and NCW electrodes cycled at a series of current rates and then at a constant rate of 0.1C.

Published on 02 2016. Downloaded by Fail Open on 23.07.25 10:02:10.

the initial three reversible (charge) capacities are 1263, 1198, and 1134 mA h g^{-1}. In order to differentiate the capacity contribution of Fe_3O_4 in the composite, the capacity contribution of the NCW is subtracted. In the initial cycles, considering the initial reversible capacity of the NCW (1200 mA h g^{-1}) and weight percentage of carbon (32%), Fe_3O_4 would contribute to a specific capacity of 1292 mA h g^{-1}, which is much higher than the theoretical capacity of Fe_3O_4. This phenomenon is commonly observed for many transition-metal oxide anodes,[43] the reasons for which are usually considered to be the reversible formation/decomposition of a polymer/gel-like solid electrolyte interphase (SEI) layer on the electrode surface or an interfacial Li^+ storage.

The rate and cycling behaviour of NCW@Fe_3O_4@NCS were evaluated by discharging/charging the electrode at a series of current rates ranging from 0.05C to 10C and then at a constant rate of 0.1C (Fig. 6c). With the increase of current rates, the capacity of NCW@Fe_3O_4@NCS shows a stepwise decrease. Nonetheless, even at the high current rates of 1, 3, 5, and 10C, this hybrid material still possesses a capacity of 619, 499, 471, and 426 mA h g^{-1}, respectively. When the current is returned to 0.1C, the capacity of NCW@Fe_3O_4@NCS drastically increases to 1007 mA h g^{-1}, indicating that it is tolerant of a high-rate operation. During the subsequent long-term cycling at 0.1C, the capacity continues to increase gradually, achieving a capacity of 1357 mA h g^{-1} in the 150th cycle. The capacity increase of metal oxide-type anodes is commonly ascribed to the activation process of active materials or the growth of a polymer/gel-like SEI film caused by the decomposition of the electrolyte. The electrochemical impedance spectra changes of NCW@Fe_3O_4@NCS electrodes during electrochemical cycling are shown in Fig. 7a. The charge-transfer resistance of the electrodes, which is reflected by the diameter of the semicircle at the high-to-middle frequency, increases gradually during the initial 10 cycles. Since the activation process of active materials usually leads to a decrease of cell resistance, the increase of resistance can be correlated to the gradual build-up of a polymer/gel-like SEI film on the electrode surface. The SEI layer could not only improve the mechanical cohesion of active materials, but also allow the reversible storage/release of Li^+ ions.

In contrast, the capacity of the NCW decreases very quickly during both the rate and cycling testing, suggesting the poor reversibility of the porous NCW for Li^+ storage. Another two control samples, bulk Fe_3O_4 and core–shell NCW@Fe_3O_4, were also prepared to compare their electrochemical performances with that of NCW@Fe_3O_4@NCS. Their SEM and TEM images are shown in Fig. S10 and S11.† The initial reversible capacity of bulk Fe_3O_4 (959 mA h g^{-1}) is much lower than that of NCW@Fe_3O_4@NCS, and the capacity drastically decreases to 434 mA h g^{-1} after 100 cycles (Fig. S12 and S13†). The large particle size and poor electronic conductivity of bulk Fe_3O_4 is believed to be related to its bad performance. In the case of core–shell NCW@Fe_3O_4, the reversible capacities and coulombic efficiencies are slightly lower than those of sandwich-like NCW@Fe_3O_4@NCS (Fig. S14†). During the cycling tests (Fig. 6c), the capacity of NCW@Fe_3O_4 begins to decline after 100 cycles, in sharp contrast to the extremely stable capacity of NCW@Fe_3O_4@NCS. On the basis of these comparative results, the good performance of NCW@Fe_3O_4@NCS can be correlated to its unique structure and composition in several aspects. (i) The 3D interconnected and porous nanowebs can provide continuous electron conduction pathways in all directions, and meanwhile facilitate the transport of Li^+ ions (see the schematic in Fig. 7b). The high surface area of NCW@Fe_3O_4@NCS (122 m^2 g^{-1}) (Fig. S15†) also offers a large electrode/electrolyte contact interface for the charge-transfer reaction. (ii) The 3D nanoweb skeleton can effectively buffer the internal stress induced by the volume variation of electrode materials during the lithiation/delithiation process, and benefit the structural stability and integrity of the electrode. (iii) The small size of Fe_3O_4 nanocrystallites as well as their uniform distribution on the NCW can greatly improve the utilization efficiency of active Fe_3O_4 materials. (iv) The uniform and continuous surface coating of PDA-derived carbon not only improves the surface electronic conductivity, but also prevents the aggregation and pulverization of Fe_3O_4 nanocrystallites.[44,45] (v) Both the PPy- and PDA-derived carbons are doped with nitrogen, which can enhance the electrochemical reactivity, electronic conductivity, and Li-ion permeability of carbon materials. (vi) The outer carbon shell favors the formation of a stable SEI layer on the electrode surface, thereby increasing the coulombic efficiency during discharge/charge cycling. TEM was used to observe the morphological changes of the NCW@Fe_3O_4@NCS electrode after 150 discharge/charge cycles (Fig. 7c). Obviously, the iron oxide nanocrystallites are firmly anchored on the 3D nanoweb, and the 1D sandwiched nanocable structure is perfectly maintained. Besides, a polymer/gel-like SEI layer is formed on the surface of the nanocables. The abovementioned structural advantages of NCW@Fe_3O_4@NCS contribute to its high capacity, high rate behavior, and good cycling performances.

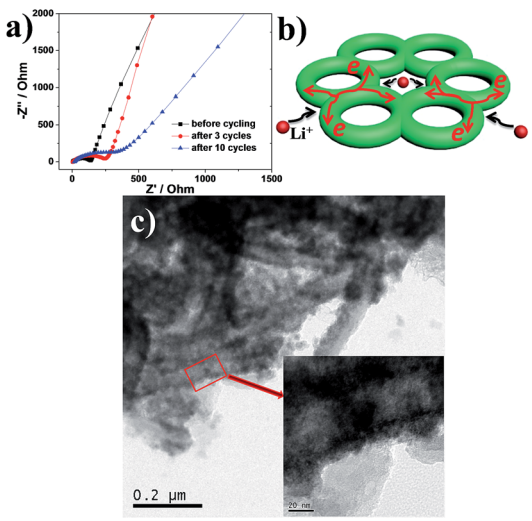

Fig. 7 The electrochemical impedance spectra changes of NCW@Fe_3O_4@NCS electrode during cycling, (b) schematic illustration of the structural advantages of the 3D nanoweb, (c) TEM images of the NCW@Fe_3O_4@NCS electrode after 150 discharge/charge cycles.

 This journal is © The Royal Society of Chemistry 2016

Published on 02 2016. Downloaded by Fail Open on 23.07.25 10:02:10.

Conclusions

In summary, a general and facile strategy is developed to fabricate sandwich-like and coaxial carbon@Fe_3O_4@carbon nanocables with the assistance of a layer-by-layer assembled polyelectrolyte. The synthesis procedure is environmentally friendly and suitable for large-scale operations. In the as-prepared 3D NCW@Fe_3O_4@NCS hybrid, the synergistic effect of the inner nitrogen-doped carbon nanoweb, the intermediate Fe_3O_4 nanocrystallites, and the outer nitrogen-doped carbon shell brings about enhanced Li-storage properties for LIBs. It is expected that this synthesis strategy could be further applied to the rational design and nanoengineering of a large variety of carbon-encapsulated functional composites for applications in energy storage, electrocatalysis, optoelectronics, and many other fields.

Experimental section

Preparation of the NCW

The nanoweb-like PPy precursor was first fabricated using a reported method but with a modified concentration of raw materials.[40] In a typical experiment, 0.8 g of cetrimonium bromide (CTAB) was dissolved in 240 mL of HCl solution (1 mol L^{-1}) in an ice bath (0–3 °C) to form a transparent solution. 1.2 g of ammonium persulfate was then added into the above solution with magnetic stirring, and a white suspension was formed immediately. 1.6 mL of a pyrrole monomer was dropwise added into the as-prepared white suspension. After being stirred for 3 h, the obtained black mixture was filtered and washed with deionized water until the filtrate became colorless and neutral. The obtained PPy precursor was dried at 60 °C under vacuum for 12 h. Finally, the NCW was prepared by calcining PPy at 650 °C for 3 h under Ar flow.

Preparation of NCW@FeOOH

The NCW was first coated with two layers of the polyelectrolyte according to our previously reported procedure.[13] The polyelectrolyte-coated NCW (30 mg) was then dispersed into 60 mL of aqueous solution containing 0.26 g of $FeCl_3 \cdot 6H_2O$ by sonication for 30 minutes. The reaction mixture was heated to 80 °C in an oil bath. After reaction for 30 minutes, the product NCW@FeOOH was collected by centrifugation, washed with distilled water and ethanol, and dried at 60 °C under vacuum for 12 h.

Preparation of NCW@Fe_3O_4@NCS, NCW@Fe_3O_4, and bulk Fe_3O_4

0.2 g of NCW@FeOOH was dispersed in 200 mL of Tris buffer aqueous solution (0.025 mol L^{-1}) to form a suspension. Subsequently, 0.08 g of dopamine was added into the mixture, which was continuously stirred for 12 h at room temperature. NCW@FeOOH@PDA was then obtained after the polymerization of dopamine. To obtain sandwiched NCW@Fe_3O_4@NCS, the as-prepared NCW@FeOOH@PDA was heated to 500 °C at a rate of 1 °C min^{-1} under an Ar flow and maintained at this temperature for 3 h. Core–shell NCW@Fe_3O_4 was prepared by calcining NCW@FeOOH directly at 500 °C under an Ar flow. Bulk Fe_3O_4 was prepared by calcining $Fe(NO_3)_3 \cdot 9H_2O$ in air at 350 °C for 3 h and then under an 8% H_2/Ar atmosphere at 500 °C for 3 h.

Preparation of 1D carbon nanotube@Fe_3O_4@NCS and carbon nanofiber@Fe_3O_4@NCS

The other two types of 1D sandwich-like C@Fe_3O_4@C composites were prepared through the similar polyelectrolyte-assisted approach except that 1D carbon nanotubes and electrospun carbon nanofibers were used as the carbon substrates, respectively.

Acknowledgements

This work was supported by the National Natural Science Foundation of China (NSFC no. 21543010, 21203133, 21301124, 21473120, and 51272168).

Notes and references

1 Y. L. Ding, Y. R. Wen, C. Wu, P. A. van Aken, J. Maier and Y. Yu, *Nano Lett.*, 2015, **15**, 1388–1394.
2 Y. P. Zhou, X. H. Rui, W. P. Sun, Z. C. Xu, Y. Zhou, W. J. Ng, Q. Y. Yan and E. Fong, *ACS Nano*, 2015, **9**, 4628–4635.
3 J. C. Ye, A. C. Baumgaertel, Y. M. Wang, J. Biener and M. M. Biener, *ACS Nano*, 2015, **9**, 2194–2202.
4 Z. M. Wan, J. Shao, J. J. Yun, H. Y. Zheng, T. Gao, M. Shen, Q. T. Qu and H. H. Zheng, *Small*, 2014, **10**, 4975–4981.
5 K. N. Zhao, L. Zhang, R. Xia, Y. F. Dong, W. W. Xu, C. J. Niu, L. He, M. Y. Yan, L. B. Qu and L. Q. Mai, *Small*, 2016, **12**, 588–594.
6 Q. T. Qu, J. M. Chen, X. X. Li, T. Gao, J. Shao and H. H. Zheng, *J. Mater. Chem. A*, 2015, **3**, 18289–18295.
7 K. Feng, W. Ahn, G. Lui, H. W. Park, A. G. Kashkooli, G. P. Jiang, X. L. Wang, X. C. Xiao and Z. W. Chen, *Nano Energy*, 2016, **19**, 187–197.
8 C. R. Ma, W. M. Zhang, Y. S. He, Q. Gong, H. Y. Che and Z. F. Ma, *Nanoscale*, 2016, **8**, 4121–4126.
9 X. Y. Zhou, T. Bai, F. Chen, J. J. Tang, Q. C. Liao, Y. R. Zhao and J. Yang, *RSC Adv.*, 2016, **6**, 19522–19530.
10 H. B. Wu, G. Zhang, L. Yu and X. W. Lou, *Nanoscale Horiz.*, 2016, **1**, 27–40.
11 X. Cao, X. Y. Chuan, R. C. Masse, D. B. Huang, S. Li and G. Z. Cao, *J. Mater. Chem. A*, 2015, **3**, 22739–22749.
12 X. X. Li, X. Y. Zheng, J. Shao, T. Gao, Q. Shi and Q. T. Qu, *Chem.–Eur. J.*, 2016, **22**, 376–381.
13 Q. T. Qu, F. Qian, S. M. Yang, T. Gao, W. J. Liu, J. Shao and H. H. Zheng, *ACS Appl. Mater. Interfaces*, 2016, **8**, 1398–1405.
14 B. Qiu, M. Xing and J. Zhang, *J. Am. Chem. Soc.*, 2014, **136**, 5852–5855.
15 Y. Zuo, G. Wang, J. Peng, G. Li, Y. Ma, F. Yu, B. Dai, X. Guo and C.-P. Wong, *J. Mater. Chem. A*, 2016, **4**, 2453–2460.
16 Q. Qu, T. Gao, H. Zheng, X. Li, H. Liu, M. Shen, J. Shao and H. Zheng, *Carbon*, 2015, **92**, 119–125.

Published on 02 2016. Downloaded by Fail Open on 23.07.25 10:02:10.

17 X. Y. Wu, S. M. Li, B. Wang, J. H. Liu and M. Yu, *Phys. Chem. Chem. Phys.*, 2016, **18**, 4505–4512.
18 J. Q. Shan, Y. X. Liu, P. Liu, Y. S. Huang, Y. Z. Su, D. Q. Wu and X. L. Feng, *J. Mater. Chem. A*, 2015, **3**, 24148–24154.
19 W. H. Xie, S. Y. Li, S. Y. Wang, S. Xue, Z. J. Liu, X. Y. Jiang and D. Y. He, *ACS Appl. Mater. Interfaces*, 2014, **6**, 20334–20339.
20 Y. Hou, J. Y. Li, Z. H. Wen, S. M. Cui, C. Yuan and J. H. Chen, *Nano Energy*, 2015, **12**, 1–8.
21 L. Xia, S. Q. Wang, G. X. Liu, L. X. Ding, D. D. Li, H. H. Wang and S. Z. Qiao, *Small*, 2016, **12**, 853–859.
22 Z. Y. Wang, D. Y. Luan, S. Madhavi, Y. Hu and X. W. Lou, *Energy Environ. Sci.*, 2012, **5**, 5252–5256.
23 Y. T. Zuo, G. Wang, J. Peng, G. Li, Y. Q. Ma, F. Yu, B. Dai, X. H. Guo and C. P. Wong, *J. Mater. Chem. A*, 2016, **4**, 2453–2460.
24 L. L. Wang, J. W. Liang, Y. C. Zhu, T. Mei, X. Zhang, Q. Yang and Y. T. Qian, *Nanoscale*, 2013, **5**, 3627–3631.
25 C. Ding, Y. Zeng, L. Cao, L. Zhao and Q. Meng, *ACS Appl. Mater. Interfaces*, 2016, **8**, 7977–7990.
26 Z. Liu, X.-Y. Yu and U. Paik, *Adv. Energy Mater.*, 2016, **6**, 1502318.
27 L. Zhao, M. M. Gao, W. B. Yue, Y. Jiang, Y. Wang, Y. Ren and F. Q. Hu, *ACS Appl. Mater. Interfaces*, 2015, **7**, 9709–9715.
28 J. N. Zhang, K. X. Wang, Q. Xu, Y. C. Zhou, F. Y. Cheng and S. J. Guo, *ACS Nano*, 2015, **9**, 3369–3376.
29 Y. C. Jiao, D. D. Han, L. M. Liu, L. Ji, G. N. Guo, J. H. Hu, D. Yang and A. G. Dong, *Angew. Chem., Int. Ed.*, 2015, **54**, 5727–5731.
30 Y. R. Wang, L. Zhang, X. H. Gao, L. Y. Mao, Y. Hu and X. W. Lou, *Small*, 2014, **10**, 2815–2819.
31 J. P. Zhao, B. J. Yang, Z. M. Zheng, J. Yang, Z. Yang, P. Zhang, W. C. Ren and X. B. Yan, *ACS Appl. Mater. Interfaces*, 2014, **6**, 9890–9896.
32 S. Han, X. J. Wang, Y. S. Huang, Y. P. Tang, Y. N. Ai, J. Z. Jiang and D. Q. Wu, *RSC Adv.*, 2015, **5**, 98399–98403.
33 L. Wang, L. Zhuo, C. Zhang and F. Zhao, *Chem.–Eur. J.*, 2014, **20**, 4308–4315.
34 Z. Y. Wu, H. W. Liang, L. F. Chen, B. C. Hu and S. H. Yu, *Acc. Chem. Res.*, 2016, **49**, 96–105.
35 S. Xin, Y. G. Guo and L. J. Wan, *Acc. Chem. Res.*, 2012, **45**, 1759–1769.
36 Z. Sun, H. Yuan, Z. Liu, B. Han and X. Zhang, *Adv. Mater.*, 2005, **17**, 2993–2997.
37 N. Du, H. Zhang, B. D. Chen, X. Y. Ma, Z. H. Liu, J. B. Wu and D. R. Yang, *Adv. Mater.*, 2007, **19**, 1641–1645.
38 Y. L. Liu, K. L. Ai and L. H. Lu, *Chem. Rev.*, 2014, **114**, 5057–5115.
39 C. Y. Zhao, X. Wang, J. H. Kong, J. M. Ang, P. S. Lee, Z. L. Liu and X. H. Lu, *ACS Appl. Mater. Interfaces*, 2016, **8**, 2372–2379.
40 Y. Wang, X. Ding, F. Wang, J. Li, S. Song and H. Zhang, *Chem. Sci.*, 2016, DOI: 10.1039/c5sc04668h.
41 L. Qie, W. M. Chen, Z. H. Wang, Q. G. Shao, X. Li, L. X. Yuan, X. L. Hu, W. X. Zhang and Y. H. Huang, *Adv. Mater.*, 2012, **24**, 2047–2050.
42 X. Lu, R. Wang, Y. Bai, J. Chen and J. Sun, *J. Mater. Chem. A*, 2015, **3**, 12031–12037.
43 J. Shao, Z. M. Wan, H. M. Liu, H. Y. Zheng, T. Gao, M. Shen, Q. T. Qu and H. H. Zheng, *J. Mater. Chem. A*, 2014, **2**, 12194–12200.
44 H. S. Li, L. F. Shen, K. B. Yin, J. Ji, J. Wang, X. Y. Wang and X. G. Zhang, *J. Mater. Chem. A*, 2013, **1**, 7270–7276.
45 C. Lei, F. Han, D. Li, W. C. Li, Q. Sun, X. Q. Zhang and A. H. Lu, *Nanoscale*, 2013, **5**, 1168–1175.

 This journal is © The Royal Society of Chemistry 2016